Available online at www.sciencedirect.com
ScienceDirect
Journal of Computational Physics 222 (2007) 720–739
JOURNAL OF COMPUTATIONAL PHYSICS
www.elsevier.com/locate/jcp

An explicit method for the nonlinear interaction between water waves and variable and moving bottom topography

Dorian Fructus, John Grue *

Mechanics Division, Department of Mathematics, University of Oslo, P.O. Box 1053, Blindern, 0316 Oslo, Norway

Received 9 March 2006; received in revised form 16 August 2006; accepted 17 August 2006
Available online 10 October 2006

Abstract

A fully nonlinear and fully dispersive method for the interaction between free surface waves and a variable bottom topography in space and time in three dimensions is derived. A Green function potential formulation expresses the normal velocity of the free surface in terms of the bathymetry and its motion. An explicit, fast version of the method is derived in Fourier space with evaluations using FFT. Practice shows that the explicit method captures the most essential parts of the wave field. This leads to a time-integration that is very accurate and orders of magnitude faster than existing full potential formulation methods. Fully resolved simulations of the nonlinear and dispersive wave fields are enabled from the generation to the shoaling of the waves, including the onshore flow which is handled by suitable numerical beaches.

Keywords: Nonlinear tsunamis by FFT; Wave-bottom interaction; Waves by slides; Waves by tectonic motion; Boundary integral formulation; Tsunami; Fully nonlinear; Three-dimensional; Explicit spectral method

1. Introduction

The modelling of nonlinear motion of water waves interacting with a fixed, variable and/or moving bottom topography is important from both the fundamental and practical points of view. Models that resolve the fully nonlinear and dispersive wave effects are important to free surface flows generated by slide motion, see e.g. [8,18,23]. The mechanics of the sliding masses is important as well [25]. The transformation of tsunami waves moving over strongly variable topography including deep and shallow regions and the detailed formation process of solitary waves as the tsunami waves move from the deep to shallow sea are still unclear. It has been suggested that fully nonlinear and fully dispersive models are required to properly resolve these issues.

The extended Boussinesq models have been improved during the last decade by using the velocity at a certain depth as a dependent variable, as introduced by Nwogo [22]. By using this trick, Wei et al. [28] were able to achieve a wider range of validity of their two-dimensional model over the entire range of water depths. The method by Nwogu was used to improve the three-dimensional highly nonlinear and dispersive Boussinesq

* Corresponding author.
E-mail addresses: dorianf@math.uio.no (D. Fructus), johng@math.uio.no (J. Grue).

0021-9991/$ - see front matter
doi:10.1016/j.jcp.2006.08.014

models [2,21,20] and was employed by Lynett and Liu [19] to derive an improved model for the study of slide generated tsunamis and the run-up. In the latter study a weak frequency dispersion was assumed, while the full effect of nonlinearity was included. The representation of nonlinearity and dispersion has recently been improved by Grilli et al. [14] developing a higher-order boundary element method for potential flow over uneven and moving topography in three dimensions. Their simulations of the nonlinear waves generated by slide agrees favorably with a set of physical wave tank experiments.

Computationally efficient methods for steep ocean surface waves in three dimensions over otherwise flat bottom have witnessed recent developments. This includes the method by Clamond and Grue [5] and Grue [15] using integral equations and analytical inversion by Fourier transform, and the method by Bateman et al. [3] generalizing the two-dimensional nonlinear pseudo spectral method by Craig and Sulem [7] to three-dimensions. Craig and Sulem's method consists in the inversion of a differential operator, using expansions, connecting the free surface potential and the normal velocity of the free surface. The methods were derived for the cases of infinite or constant, finite water depth. Bateman et al. performed numerical simulations of directionally spread surface water waves, while, Gibson and Swan [12] used the method (and that of Zakharov [30]) to study focusing wave events in unidirectional and directional sea-states. Recently, Ablowitz et al. [1] derived an integral formulation using exponentials. The latter results from a transform of the Rankine singularity and is similar to the Green function method explored here. Their formulation is valid also for the case of an uneven bottom. The authors used their formulation to derive, in the case of finite, constant water depth, the two-dimensional Boussinesq, Benney–Luke, and Kadomtsev–Petviashvili equations, and in the case of infinite water depth, the nonlinear Schrödinger equation. They computed traveling solitary-lump wave solutions for the Benney–Luke and the full equations (in the case of weak nonlinearity and weak dispersion) using a computational fixed point method. No computations were given for wave motion over uneven non-moving bottom. The recent generalized Boussinesq method and the integral equation formulation alternative have recently been employed to compute steep three-dimensional wave patterns at constant water depth [9–11].

A somewhat related method to ours is the operator-expansion formalism explored by Smith [26]. This is an extension of the Hamilton formulation by Watson and West [27] to wave motion over non-moving variable bottom in three dimensions. Smith compared his simulations with the shoaling experiments of Wei et al. [28] finding an accuracy similar to the extended Boussinesq models. For the case of two-dimensional wave motion over flat bottom the method by Smith reduces to the model by Craig and Sulem [7].

In this paper, we derive an explicit formulation and describe a corresponding numerical implementation for the simulation of water waves that are driven by an arbitrary motion of the sea bottom, or wave motion propagating over an uneven bottom topography, in three dimensions. The formulation assumes the application of potential theory and is fully nonlinear and fully dispersive. A set of integral equations is derived. This connects the (unknown) normal velocity at the free surface, V_s, and the (unknown) fluid potential at the moving sea bottom, ϕ_b, to the (known) free surface potential, ϕ_s, and the (known) normal velocity of the sea bottom, V_b. The integral equations are inverted by the use of Fourier transform. The subsequent relations are derived in Fourier space. The relations are brought on a form that is suitable for the method of successive approximations, which leads to a convergent final result. In the first approximation we arrive at the linear equations in Fourier space. With the linear part of the prognostic equations integrated analytically, the equations yield the wave field at any time instant on analytical form and fits with the linear formulas derived by Hammack [17]. Higher analytical approximations to the equations for V_s and ϕ_b are derived. The equations become on a form where a global, dominant part of the solution is explicit (and is obtained without any equation solving). Its evaluation is performed by the use of FFT and is therefore very rapid. This part of the solution may be improved by performing iterations, but practice shows that the method converges so rapidly that the explicit version is highly useful. There is also a local part of the solution which is evaluated by rapidly convergent integrals. This local contribution involves high-order products between the components of the wave field and rapidly decaying kernels. The contribution is very small.

The scarcity of fully nonlinear 3D wave computations of landslide tsunami sources, and otherwise wave motion over variable bathymetry, motivates for the derivation of alternative simulation methods and model studies of the phenomenon. It is well known that full methods in 3D are slow, and that steps should be taken to improve the computational performance of the models. This has stimulated our interest in the derivation of

analytic equations for fast and robust simulations of strongly nonlinear ocean surface waves interacting the fixed or moving bottom topography. We shall find that our method reproduces well the physical and numerical experiments by Grilli et al. [14]. An important point is that the computing time, using the present formulation, is several factors smaller (one in eighteen thousand in the actual comparison). We also compute the strongly nonlinear shoaling of solitary waves, up to the point of breaking, where breaking is realized by numerical growth of the high-frequency part of the wave spectrum. The numerical breaking corresponds to physical breaking when the computational results are independent of resolution. It is important to note that in the present formulation, no smoothing or regridding is used, and a zeros-padding technique is implemented to avoid aliasing in the computation of cubic products.

2. Mathematical formulation

We study the nonlinear motion of a free surface in three-dimensions. The fluid is assumed to be homogeneous and incompressible, and the motion irrotational. The water depth is finite, and the bottom is allowed to vary in space and time.

2.1. Prognostic equations

Let $\boldsymbol{x} = (x_1, x_2)$ denote the horizontal coordinate, y the vertical coordinate and t time. Let $y = 0$ represent the still water level and $y = \eta(\boldsymbol{x}, t)$ the surface elevation. The vertical position of the time-variable sea bottom is represented by $y = -h + \delta(\boldsymbol{x}, t)$, where in the special case of a flat bottom located at $y = -h$, the field $\delta(\boldsymbol{x}, t)$ is identically zero. Let ϕ denote the velocity potential, $\boldsymbol{\nabla} = (\partial/\partial x_1, \partial/\partial x_2)$ the horizontal gradient and grad ϕ the three-dimensional velocity field. We shall use the subscript 's' to denote quantities at the free surface, e.g. $\phi_s(\boldsymbol{x}, t) = \phi(\boldsymbol{x}, y = \eta(\boldsymbol{x}, t), t)$, and the subscript 'b' to denote quantities at the sea bottom, e.g. $\phi_b(\boldsymbol{x}, t) = \phi(\boldsymbol{x}, y = -h + \delta(\boldsymbol{x}, t), t)$.

The kinematic and dynamic conditions at the free surface can be written as [15, Eqs. (3) and (4)]:

$$\partial\eta/\partial t - V_s = 0, \quad \text{where } V_s = \partial\phi/\partial n/\sqrt{1 + |\boldsymbol{\nabla}\eta|^2}, \tag{1}$$

$$\partial\phi_s/\partial t + g/\eta + \frac{|\nabla\phi_s|^2 - V_s^2 - 2V_s\nabla\eta\cdot\nabla\phi_s + |\nabla\eta\times\nabla\phi_s|^2}{2(1+|\nabla\eta|^2)} = 0, \tag{2}$$

where the unit normal vector, $\vec{n}$, is pointing out of the fluid and g denotes the acceleration of gravity. In (2), the effects of a surface tension and an external pressure are not included.

The scaled normal velocity of the moving sea bottom is introduced by

$$V_b = \partial\delta/\partial t = \partial\phi/\partial n\sqrt{1 + |\boldsymbol{\nabla}\delta|^2}, \tag{3}$$

where the normal vector at the sea floor, $\vec{n}$, is chosen to point into the fluid, see Fig. 1.

Eqs. (1) and (2) are used to integrate η and ϕ_s forward in time once the (scaled) normal velocity at the free surface, V_s, and the velocity potential at the sea floor, ϕ_b, are found. The time integration procedure is

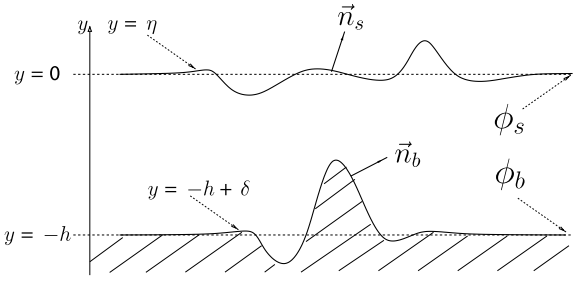

Fig. 1. Transversal cut of the model considered.

described in Appendix A.1. At each time step V_s has to be evaluated, given η, ϕ_s and the motion of the sea bottom. This implies the solution of a coupled set of integral equations for V_s and ϕ_b.

3. Solution of the Laplace equation

3.1. Field point on the free surface

Solution of the Laplace equation is obtained by applying Green's theorem to the velocity potential ϕ and a suitable source Green function. For an evaluation point that is on the free surface we obtain

$$\int_{\mathscr{S}+\mathscr{B}} \left(\frac{1}{\tilde{r}}+\frac{1}{\tilde{r}_B}\right)\frac{\partial\phi'}{\partial n_1'}\,\mathrm{d}S' = 2\pi\phi + \int_{\mathscr{S}+\mathscr{B}} \phi'\frac{\partial}{\partial n_1'}\left(\frac{1}{\tilde{r}}+\frac{1}{\tilde{r}_B}\right)\mathrm{d}S'. \tag{4}$$

Here, $\tilde{r}^2 = R^2 + (y'-y)^2$, $\tilde{r}_B^2 = R^2 + (y'+y+2h)^2$, $\mathbf{R} = \boldsymbol{x}' - \boldsymbol{x}$, and $R = |\boldsymbol{x}' - \boldsymbol{x}|$ denotes the horizontal distance between the primed and unprimed positions. Further, $\mathscr{S}$ denotes the instantaneous free surface and $\mathscr{B}$ the instantaneous surface of the sea bottom. The normal n_1 is pointing out of the fluid ($n = n_1$ at the free surface, and $n = -n_1$ at the sea-floor). In (4) we have assumed that there is no motion in the far-field.

We assume that $\mathscr{S}$ and $\mathscr{B}$ are single-valued surfaces and are parameterized by the $\boldsymbol{x}$-coordinate. We introduce $\mathrm{d}S' = \sqrt{1+|\nabla'\eta'|^2}\,\mathrm{d}\boldsymbol{x}'$ at the free surface $\mathscr{S}$ and $\mathrm{d}S' = \sqrt{1+|\nabla'\delta'\|^2}\,\mathrm{d}\boldsymbol{x}'$ at the bottom surface $\mathscr{B}$. For the notation we use $\eta' = \eta(\boldsymbol{x}', t)$, $\eta = \eta(\boldsymbol{x}, t)$, $\delta' = \delta(\boldsymbol{x}', t)$ and $\delta = \delta(\boldsymbol{x}, t)$. The integral equation may be expressed on the form

$$\begin{aligned}\int_{\mathscr{S}} \left(\frac{1}{\tilde{r}}+\frac{1}{\tilde{r}_B}\right)V_s'\,\mathrm{d}\boldsymbol{x}' = 2\pi\phi_s &+ \int_{\mathscr{B}} \left(\frac{1}{\tilde{r}}+\frac{1}{\tilde{r}_B}\right)V_b'\,\mathrm{d}\boldsymbol{x}' + \int_{\mathscr{S}} \phi_s'\frac{\partial}{\partial n'}\left(\frac{1}{\tilde{r}}+\frac{1}{\tilde{r}_B}\right)\sqrt{1+|\nabla'\eta'|^2}\,\mathrm{d}\boldsymbol{x}' \\ &- \int_{\mathscr{B}} \phi_b'\frac{\partial}{\partial n'}\left(\frac{1}{\tilde{r}}+\frac{1}{\tilde{r}_B}\right)\sqrt{1+|\nabla'\delta'|^2}\,\mathrm{d}\boldsymbol{x}',\end{aligned} \tag{5}$$

which is valid on the free surface at $y = \eta(\boldsymbol{x}, t)$. For a flat bottom the last term in (5) vanishes. The choice of the image through $\tilde{r}_B$ ensures a robust evaluation of all the terms on the r.h.s. of the equation, and the weakly singular part on the l.h.s. is handled by the use of Fourier transform, see below.

The novel additions in (5) – as compared to previous works – are the terms that account for the variation of the sea bottom in space and time, i.e. non-zero functions $\delta(\boldsymbol{x}, t)$ and $V_b(\boldsymbol{x}, t)$. More specifically new integrals include

$$\int_{\mathscr{B}} \left(\frac{1}{\tilde{r}}+\frac{1}{\tilde{r}_B}\right)V_b'\,\mathrm{d}\boldsymbol{x}', \quad -\int_{\mathscr{B}} \phi_b'\frac{\partial}{\partial n'}\left(\frac{1}{\tilde{r}}+\frac{1}{\tilde{r}_B}\right)\sqrt{1+|\nabla'\delta'\|^2}\,\mathrm{d}\boldsymbol{x}'. \tag{6}$$

We note that

$$\frac{1}{\tilde{r}}+\frac{1}{\tilde{r}_B} = \frac{2}{R_2} + 2\eta\frac{\partial}{\partial h}\frac{1}{R_2} + (\delta'^2+\eta^2)\frac{\partial^2}{\partial h^2}\frac{1}{R_2} + \frac{1}{\mathscr{R}_1}, \tag{7}$$

where $R_2^2 = R^2 + h^2$ (and $R = |\boldsymbol{x}' - \boldsymbol{x}|$). The three first terms on the right of (7) are the leading terms of the singularities on the left of (7). The remaining part is defined by the difference, i.e.

$$\frac{1}{\mathscr{R}_1} = \frac{1}{\tilde{r}}+\frac{1}{\tilde{r}_B} - \frac{2}{R_2} - 2\eta\frac{\partial}{\partial h}\frac{1}{R_2} - (\delta'^2+\eta^2)\frac{\partial^2}{\partial h^2}\frac{1}{R_2}$$

and is a small quantity, decaying rapidly with R.

Now, we use that

$$\frac{\partial^n}{\partial h^n}\frac{1}{R_2} = \mathfrak{F}^{-1}\left\{\frac{2\pi(-k)^n}{k}\mathrm{e}^{-\mathrm{i}\boldsymbol{k}\cdot\boldsymbol{x}'-kh}\right\}, \tag{8}$$

where $\boldsymbol{k}$ denotes the wavenumber in Fourier space, $k = |\boldsymbol{k}|$, $\mathfrak{F}$ denotes Fourier transform and $\mathfrak{F}^{-1}$ the inverse transform. We evaluate the integral

$$\int_{\mathscr{B}}\left(\frac{1}{\tilde{r}}+\frac{1}{\tilde{r}_{\mathrm{B}}}\right)V'_{\mathrm{b}}\,\mathrm{d}\boldsymbol{x}'=\mathfrak{F}^{-1}\{4\pi\mathrm{e}^{-kh}\mathfrak{F}(V_{\mathrm{b}})/k\}-\eta\mathfrak{F}^{-1}\{4\pi\mathrm{e}^{-kh}\mathfrak{F}(V_{\mathrm{b}})\}+\mathfrak{F}^{-1}\{2\pi k\mathrm{e}^{-kh}\mathfrak{F}(\delta^2V_{\mathrm{b}})\}$$
$$+\eta^2\mathfrak{F}^{-1}\{2\pi k\mathrm{e}^{-kh}\mathfrak{F}(V_{\mathrm{b}})\}+\int_{\mathscr{B}}\left(\frac{1}{\mathscr{R}_1}\right)V'_{\mathrm{b}}\,\mathrm{d}\boldsymbol{x}'. \tag{9}$$

To evaluate the second integral in (6) we first note that

$$\sqrt{1+|\nabla'\delta'|^2}\,\frac{\partial}{\partial n'}\left(\frac{1}{\tilde{r}}+\frac{1}{\tilde{r}_{\mathrm{B}}}\right)=-\frac{-\boldsymbol{R}\cdot\nabla'\delta'+y'-y}{\tilde{r}^3}-\frac{-\boldsymbol{R}\cdot\nabla'\delta'+y'+y+2h}{\tilde{r}_{\mathrm{B}}^3}, \tag{10}$$

where $y'=-h+\delta'$ (on the sea floor) and $y=\eta$ (on the sea surface). The r.h.s. of the equation may be developed to

$$\sqrt{1+|\nabla'\delta'|^2}\,\frac{\partial}{\partial n'}\left(\frac{1}{\tilde{r}}+\frac{1}{\tilde{r}_{\mathrm{B}}}\right)=-2\nabla'\cdot\left(\delta'\nabla'\frac{1}{R_2}\right)-2\eta\nabla'\cdot\left(\delta'\nabla'\frac{\partial}{\partial h}\frac{1}{R_2}\right)+\frac{1}{\mathscr{R}_2}, \tag{11}$$

where the two first terms on the right give the leading contribution to the left-hand side, and $1/\mathscr{R}_2$ is a small remainder.

We then obtain for the integral

$$-\int_{\mathscr{B}}\phi'_{\mathrm{b}}\frac{\partial}{\partial n}\left(\frac{1}{\tilde{r}}+\frac{1}{\tilde{r}_{\mathrm{B}}}\right)\sqrt{1+|\nabla'\delta'|^2}\,\mathrm{d}\boldsymbol{x}'=\mathfrak{F}^{-1}\{4\pi\mathrm{i}\mathrm{e}^{-kh}(\boldsymbol{k}/k)\cdot\mathfrak{F}(\delta\nabla\phi_{\mathrm{b}})\}-\eta\mathfrak{F}^{-1}\{4\pi\mathrm{i}\mathrm{e}^{-kh}\boldsymbol{k}\cdot\mathfrak{F}(\delta\nabla\phi_{\mathrm{b}})\}$$
$$-\int_{\mathscr{B}}\left(\frac{1}{\mathscr{R}_2}\right)\phi'_{\mathrm{b}}\,\mathrm{d}\boldsymbol{x}'. \tag{12}$$

The integral equation corresponding to (5), for the case of a non-moving horizontal sea floor, at constant level $y=-h$, i.e. $\delta=0$ and $V_{\mathrm{b}}=0$, was derived in [15, Eq. (35)]. Adding the two new contributions, given in Eqs. (9) and (12), we obtain

$$\mathfrak{F}^{-1}\left\{\frac{1+e_h}{k}[\mathfrak{F}(V_{\mathrm{s}})+\mathrm{i}\boldsymbol{k}\cdot\mathfrak{F}(\eta\nabla\phi_{\mathrm{s}})]\right\}=\mathfrak{F}^{-1}\{(1-e_h)\mathfrak{F}(\phi_{\mathrm{s}}-\eta V_{\mathrm{s}}^{(1)})\}+T(\phi_{\mathrm{s}})+T_1(\phi_{\mathrm{s}})+N(V_{\mathrm{s}})$$
$$+N_1(V_{\mathrm{s}})+\mathfrak{F}^{-1}\{e_h\mathfrak{F}(\eta(V_{\mathrm{s}}-V_{\mathrm{s}}^{(1)}))\}+\eta\mathfrak{F}^{-1}(e_h\mathfrak{F}(V_{\mathrm{s}}-V_{\mathrm{s}}^{(1)}))$$
$$+\mathfrak{F}^{-1}\left\{\frac{2\sqrt{e_h}\mathfrak{F}(V_{\mathrm{b}})}{k}\right\}-\eta\mathfrak{F}^{-1}\{2\sqrt{e_h}\mathfrak{F}(V_{\mathrm{b}})\}+\mathfrak{F}^{-1}\{k\sqrt{e_h}\mathfrak{F}(\delta^2V_{\mathrm{b}})\}$$
$$+\eta^2\mathfrak{F}^{-1}\{k\sqrt{e_h}\mathfrak{F}(V_{\mathrm{b}})\}+\mathfrak{F}^{-1}\left\{\frac{\mathrm{i}\boldsymbol{k}}{k}\cdot2\sqrt{e_h}\mathfrak{F}(\delta\nabla\phi_{\mathrm{b}})\right\}$$
$$-\eta\mathfrak{F}^{-1}\{2\mathrm{i}\sqrt{e_h}\boldsymbol{k}\cdot\mathfrak{F}(\delta\nabla\phi_{\mathrm{b}})\}+\int_{\mathscr{B}}\left(\frac{1}{\mathscr{R}_1}\right)V'_{\mathrm{b}}\,\mathrm{d}\boldsymbol{x}'-\int_{\mathscr{B}}\left(\frac{1}{\mathscr{R}_2}\right)\phi'_{\mathrm{b}}\,\mathrm{d}\boldsymbol{x}', \tag{13}$$

where $e_h=\mathrm{e}^{-2kh}$ and $V_{\mathrm{s}}^{(1)}$ is given in Eq. (24). The functions $T(\phi_{\mathrm{s}})$, $N(V_{\mathrm{s}})$, $N_1(V_{\mathrm{s}})$ and $T_1(\phi_{\mathrm{s}})$ are given in [15, Eqs. (9), (10), (29) and (30)], respectively. In (13) we have divided by a factor of 2π.

3.2. Evaluation of the velocity potential at the bottom surface $\mathscr{B}$

An additional equation for the velocity potential ϕ_{b} at the uneven sea bottom is required in order to solve (5), and is obtained by the application of Green's theorem. In this case we employ $1/\tilde{r}+1/\tilde{r}_{\mathrm{C}}$ where $\tilde{r}^2=R^2+(y'-y)^2$ and $\tilde{r}_{\mathrm{C}}^2=R^2+(y'+y)^2$ is the image with respect with $y=0$. The resulting equation becomes

$$2\pi\phi_{\mathrm{b}}=\int_{\mathscr{S}}\left(\frac{1}{\tilde{r}}+\frac{1}{\tilde{r}_{\mathrm{C}}}\right)V'_{\mathrm{s}}\,\mathrm{d}\boldsymbol{x}'-\int_{\mathscr{B}}\left(\frac{1}{\tilde{r}}+\frac{1}{\tilde{r}_{\mathrm{C}}}\right)V'_{\mathrm{b}}\,\mathrm{d}\boldsymbol{x}'-\int_{\mathscr{S}}\phi'_{\mathrm{s}}\frac{\partial}{\partial n}\left(\frac{1}{\tilde{r}}+\frac{1}{\tilde{r}_{\mathrm{C}}}\right)\sqrt{1+|\nabla'\eta'|^2}\,\mathrm{d}\boldsymbol{x}'$$
$$+\int_{\mathscr{B}}\phi'_{\mathrm{b}}\frac{\partial}{\partial n}\left(\frac{1}{\tilde{r}}+\frac{1}{\tilde{r}_{\mathrm{C}}}\right)\sqrt{1+|\nabla'\delta'|^2}\,\mathrm{d}\boldsymbol{x}', \tag{14}$$

which is valid on the sea bottom, for $y = -h + \delta(\boldsymbol{x}, t)$. In the case of a flat free surface the integral on the r.h.s. over ϕ_s vanishes. The choice of Green function leads to a robust evaluation of the terms in the equation, where the leading part of the weakly singular function $1/\tilde{r}$ is integrated using Fourier transform.

We evaluate the terms in (14). For the integration over $\mathscr{B}$ we note

$$\frac{1}{\tilde{r}} + \frac{1}{\tilde{r}_C} = \frac{1}{R} + \frac{1}{R_1} - (\delta' + \delta)\frac{\partial}{\partial(2h)}\frac{1}{R_1} + \frac{1}{\mathscr{R}_3}, \tag{15}$$

where the first three terms on the right capture the leading behavior of the function on the left, $R_1^2 = R^2 + (2h)^2$, and $1/\mathscr{R}_3$ is a small remainder.

Further,

$$\sqrt{1 + |\nabla'\delta'|^2}\frac{\partial}{\partial n'}\left(\frac{1}{\tilde{r}} + \frac{1}{\tilde{r}_C}\right) = -\nabla' \cdot \left((\delta' - \delta)\nabla'\frac{1}{R}\right) - \nabla' \cdot \left((\delta' + \delta)\nabla'\frac{1}{R_1}\right) - \frac{\partial}{\partial(2h)}\frac{1}{R_1} + \frac{1}{\mathscr{R}_4}. \tag{16}$$

For the integration over $\mathscr{S}$ we obtain

$$\frac{1}{\tilde{r}} + \frac{1}{\tilde{r}_C} = \frac{2}{R_2} - 2\delta\frac{\partial}{\partial h}\frac{1}{R_2} + \frac{1}{\mathscr{R}_5}, \tag{17}$$

$$\sqrt{1 + |\nabla'\eta'|^2}\frac{\partial}{\partial n'}\left(\frac{1}{\tilde{r}} + \frac{1}{\tilde{r}_C}\right) = -\nabla' \cdot \left(2\eta'\nabla'\frac{1}{R_2}\right) + \frac{1}{\mathscr{R}_6}. \tag{18}$$

Now, using (8) and

$$\frac{1}{R} = \mathfrak{F}^{-1}\left\{\frac{2\pi}{k}e^{-i\boldsymbol{k}\cdot\boldsymbol{x}'}\right\}, \quad \frac{1}{R_1} = \mathfrak{F}^{-1}\left\{\frac{2\pi}{k}e^{-i\boldsymbol{k}\cdot\boldsymbol{x}' - 2kh}\right\}, \tag{19}$$

we may evaluate the integrals in (14). The equation becomes:

$$2\pi\phi_b = 2\pi\mathfrak{F}^{-1}(\mathscr{A}) + \int_{\mathscr{S}}\left(\frac{1}{\mathscr{R}_5}\right)V_s\,d\boldsymbol{x}' - \int_{\mathscr{B}}\left(\frac{1}{\mathscr{R}_3}\right)V_b\,d\boldsymbol{x}' - \int_{\mathscr{S}}\left(\frac{1}{\mathscr{R}_6}\right)\phi_s\,d\boldsymbol{x}' + \int_{\mathscr{B}}\left(\frac{1}{\mathscr{R}_4}\right)V_s\,d\boldsymbol{x}', \tag{20}$$

where

$$\begin{aligned}\mathscr{A} = {} & \frac{2\sqrt{e_h}\mathfrak{F}(V_s)}{k} + 2\delta\sqrt{e_h}\mathfrak{F}(V_s) - \frac{(1+e_h)\mathfrak{F}(V_b)}{k} - \delta e_h\mathfrak{F}(V_b) - e_h\mathfrak{F}(\delta V_b) + \frac{2i\boldsymbol{k}}{k}\cdot\sqrt{e_h}\mathfrak{F}(\eta\nabla\phi_s) \\ & + e_h\mathfrak{F}(\phi_b) - \delta(1-e_h)k\mathfrak{F}(\phi_b) - \frac{i\boldsymbol{k}}{k}\cdot(1+e_h)\mathfrak{F}(\delta\nabla\phi_b).\end{aligned} \tag{21}$$

By taking the Fourier transform on both sides of (20) we obtain

$$\begin{aligned}\mathfrak{F}(\phi_b) = {} & \mathfrak{F}(\phi_b^{(V)}) + \mathfrak{F}(\delta V_b) + \frac{i\boldsymbol{k}}{k\sinh(kh)}\cdot\mathfrak{F}(\eta\nabla\phi_s) - \frac{i\boldsymbol{k}}{k\tanh(kh)}\cdot\mathfrak{F}(\delta\nabla\phi_b) \\ & - \frac{1}{1-e_h}\mathfrak{F}(\delta\mathfrak{F}^{-1}\{k(1-e_h)[\mathfrak{F}(\phi_b) - \mathfrak{F}(\phi_b^{(1)})]\}) + \int_{\mathscr{S}}\left(\frac{1}{\mathscr{R}_5}\right)V_s\,d\boldsymbol{x}' - \int_{\mathscr{B}}\left(\frac{1}{\mathscr{R}_3}\right)V_b\,d\boldsymbol{x}' \\ & - \int_{\mathscr{S}}\left(\frac{1}{\mathscr{R}_6}\right)\phi_s\,d\boldsymbol{x}' + \int_{\mathscr{B}}\left(\frac{1}{\mathscr{R}_4}\right)V_s\,d\boldsymbol{x}',\end{aligned} \tag{22}$$

where

$$\mathfrak{F}(\phi_b^{(V)}) = \frac{\mathfrak{F}(V_s)}{k\sinh(kh)} - \frac{\mathfrak{F}(V_b)}{k\tanh(kh)}. \tag{23}$$

3.3. Successive approximations

The solution of the coupled equations (13) and (22) yields V_s and ϕ_b. Since the equations are linear in V_s and ϕ_b, a successive evaluation strategy is warranted. The iterative procedure is initiated by deriving a first approximation where η, η', δ and δ' are put to zero in (13) and (22), giving

$$\mathfrak{F}(V_s^{(1)}) = k\tanh(kh)\mathfrak{F}(\phi_s) + \frac{\mathfrak{F}(V_b)}{\cosh(kh)}, \tag{24}$$

$$\mathfrak{F}(\phi_b^{(1)}) = \frac{1}{\cosh(kh)}\mathfrak{F}(\phi_s) - \frac{\tanh(kh)}{k}\mathfrak{F}(V_b), \tag{25}$$

which determine $\mathfrak{F}(V_s^{(1)})$ and $\mathfrak{F}(\phi_b^{(1)})$ explicitly in terms of $\mathfrak{F}(\phi_s)$ and $\mathfrak{F}(V_b)$. The result (24) and (25) is independent of the choice of Green function.

For motion of small amplitude, (24) and (25) give the linear solution of the wave generation problem. We observe that the entire motion is driven by the normal velocity of the sea bottom, i.e. $V_b = \partial\phi/\partial n\sqrt{1+|\nabla\delta|^2}$. Eq. (24) expresses V_s in terms of V_b for all times and may be plugged into the linear version of the prognostic equations which is integrated analytically. In this way we obtain an explicit solution to the linear wave field generated by the motion of the moving bottom. This linear wave field has been obtained long ago and is documented in several publications, including e.g. Hammack [17]. He examined the applicability of the linear approximation in the wave generation region comparing theory and experiment finding good agreement when the total amplitude of the bed displacement was small. Our formulation gives the same analytical result as that of Hammack [17, Eq. (17)], given the same initial motion. (We note that the quantities (V_s, ϕ_s) and (V_b, ϕ_b) are evaluated at the position of the moving free surface and the moving bottom and therefore contain nonlinear components, which are small when the generation amplitude is small, however.)

An improved approximation to the nonlinear wave field is obtained by keeping terms that are linear in η, η', δ and δ', giving

$$\mathfrak{F}(V_s^{(2)}) = \mathfrak{F}(V_s^{(1)}) - \left[k\tanh(kh)\mathfrak{F}(\eta V_s^{(1)}) + \mathrm{i}\boldsymbol{k}\cdot\mathfrak{F}\{\eta\nabla\phi_s\} - \frac{1}{\cosh(kh)}\mathrm{i}\boldsymbol{k}\cdot\mathfrak{F}\{\delta\nabla\phi_b^{(1)}\}\right], \tag{26}$$

$$\mathfrak{F}(\phi_b^{(2)}) = \mathfrak{F}(\phi_b^{(1)}) - \frac{1}{\cosh(kh)}\mathfrak{F}(\eta V_s^{(1)}) - \mathrm{i}\frac{\tanh(kh)}{k}\boldsymbol{k}\cdot\mathfrak{F}\{\delta\nabla\phi_b^{(1)}\} + \mathfrak{F}(\delta V_b), \tag{27}$$

where $V_s^{(1)}$ and $\phi_b^{(1)}$ are obtained from (24) to (25). By performing another analytical iteration, keeping terms in the kernels of the integral equations that are quadratic in η, η', δ and δ', we obtain

$$\begin{aligned}\mathfrak{F}(V_s^{(3)}) = \mathfrak{F}(V_s^{(2)}) &- \left[k\tanh(kh)\mathfrak{F}(\eta(V_s^{(2)} - V_s^{(1)})) - \frac{k^2}{2}\mathfrak{F}(\eta^2 V_s^{(1)})\right] \\ &+ \frac{k}{1+e_h}\left\{\mathfrak{F}(\eta\mathfrak{F}^{-1}[-\mathrm{i}k\cdot\mathfrak{F}\{\eta\nabla\phi_s\}]) + \mathrm{i}\frac{e_h}{2}k\cdot\mathfrak{F}\{\eta^2\nabla\phi_s\} - \mathfrak{F}\left\{\eta^2\mathfrak{F}^{-1}\left[\frac{k^2}{2}\phi_s\right]\right\}\right\} \\ &+ \frac{k}{1+e_h}\left\{k\sqrt{e_h}\mathfrak{F}\{\delta^2 V_b\} + 2\mathrm{i}\frac{\sqrt{e_h}}{k}k\cdot\mathfrak{F}\{\delta\nabla(\phi_b^{(2)} - \phi_b^{(1)})\}\right\},\end{aligned} \tag{28}$$

where $V_s^{(1)}$ and $\phi_b^{(1)}$ are obtained from (24) to (25), $V_s^{(2)}$ and $\phi_b^{(2)}$ from (26) to (27) and $e_h = \exp(-2kh)$. The equations for $V_s^{(1)}$, $V_s^{(2)}$, $V_s^{(3)}$ and V_s below are valid on the exact position of the free surface. Similarly, the potential and normal velocity at the sea floor are evaluated on the exact position of the sea floor.

Both (26), (27) and (28) are independent of the choice of Green function. The latter is important for the formulas that are derived below, however.

3.4. Complete evaluation of V_s and ϕ_b

The Fourier inversion of the complete equation (5) gives

$$\mathfrak{F}(V_s) = \mathfrak{F}(V_s^{(3)}) + \mathfrak{F}(V_s^{(R,1)}) + \mathfrak{F}(V_s^{(R,2)}), \tag{29}$$

where

$$\mathfrak{F}(V_s^{(R,1)}) = -\left[k\tanh(kh)\mathfrak{F}\{\eta(V_s - V_s^{(2)})\} - \frac{\mathrm{i}}{\cosh(kh)}k\cdot\mathfrak{F}\{\delta\nabla(\phi_b - \phi_b^{(2)})\}\right] + \frac{k}{1+e_h}\mathfrak{F}(\eta\mathfrak{F}^{-1}[(1+e_h)(\mathfrak{F}(V_s) - \mathfrak{F}(V_s^{(2)}))]) + \frac{k}{1+e_h}\mathfrak{F}\left(\eta\mathfrak{F}^{-1}\left[(1+e_h)\left[k\tanh(kh)\mathfrak{F}\{\eta(V_s - V_s^{(1)})\} - \frac{\mathrm{i}}{\cosh(kh)}k\cdot\mathfrak{F}\{\delta\nabla(\phi_b - \phi_b^{(2)})\}\right]\right]\right) - \frac{k}{1+e_h}\left[\mathfrak{F}\left(\eta^2\mathfrak{F}^{-1}\left[\frac{k(1+e_h)}{2}\mathfrak{F}(V_s - V_s^{(1)})\right]\right) + \frac{k}{2}(1+e_h)\mathfrak{F}(\eta^2(V_s - V_s^{(1)}))\right], \tag{30}$$

$$\mathfrak{F}(V_s^{(R,2)}) = \frac{k}{1+e_h}\mathfrak{F}[-N^S(V_s) - N^B(V_b) + T^S(\phi_s) - T^B(\phi_b)], \tag{31}$$

where the dominant part has already been obtained in $V_s^{(3)}$.

Correspondingly, the Fourier transform of the complete equation (14) gives

$$\mathfrak{F}(\phi_b) = \mathfrak{F}(\phi_b^{(2)}) + \mathfrak{F}(\phi_b^{(R,1)}) + \mathfrak{F}(\phi_b^{(R,2)}), \tag{32}$$

$$\mathfrak{F}(\phi_b^{(R,1)}) = \frac{1}{k\sinh(kh)}\mathfrak{F}(V_s - V_s^{(2)}) - \mathrm{i}\frac{k}{k\tanh(kh)}\cdot\mathfrak{F}\{\delta\nabla(\phi_b - \phi_b^{(1)})\} - \frac{1}{1-e_h}\mathfrak{F}\left(\delta\mathfrak{F}^{-1}\left[k(1-e_h)\mathfrak{F}(\phi_b - \phi_b^{(1)}) - 2\sqrt{e_h}\mathfrak{F}(V_s - V_s^{(1)})\right]\right), \tag{33}$$

$$\mathfrak{F}(\phi_b^{(R,2)}) = \frac{1}{1-e_h}\mathfrak{F}[M^B(V_b) + S^B(V_s) + D^B(\phi_s) + P^B(\phi_b)], \tag{34}$$

where the $V_s^{(k)}$, $k = 1,2,3$, and $\phi_b^{(k)}$, $k = 1,2$, are obtained above. The functions $T^S(\phi_s)$, $N^S(V_s)$, $N^B(V_b)$, $T^B(\phi_b)$, $M^B(V_b)$, $D^B(\phi_s)$, $S^B(V_s)$ and $P^B(\phi_b)$ are integrals over highly nonlinear products of the wave motion characteristics multiplied by kernels that decay quickly with the radial distance R. The integrals have very local contributions in the x_1,x_2-plane. In the practical evaluation is suffices to integrate over rectangles (squares) with length corresponding one typical wavelength in the x_1- and x_2-directions. The functions are given in Appendix A.

The evaluation of (29) and (32) is composed by a dominant part which involves a global evaluation of the wave field and is evaluated using FFTs. Highly accurate results (see below) are obtained from the global FFT-part which also is very rapid. The remaining part is highly nonlinear, highly local, and its evaluation relatively slow. It is therefore tempting to work with the fast FFT-part which provides a highly accurate inversion of the Laplace equation. Together with the exact boundary conditions they provide a highly nonlinear and dispersive simulation model of the wave field.

We note that a larger fraction of the local contributions to V_s and ϕ_b may in principle be recast in a global FFT-form. This has been tested out for wave propagation in water of constant depth, with negative conclusion: a continued expansion of the kernels was found to lead to divergence of the otherwise stable numerical scheme [9].

4. Numerical implementation: convergence, accuracy

The part of the horizontal plane used for numerical integration has length L and width W. The number of nodes along the x_1-direction (length) is $2N_1$, and along the x_2-direction (width) $2N_2$. The reason for the factor of 2 is that we use a zeros-padding technique in the evaluation of the convolution products, where in the Fourier space, the upper N_1 and N_2 of the Fourier modes are put to zero. The effect of aliasing is then avoided in the convolution products up to cubic order. The spectrally accurate trapezoidal rule is used in the numerical evaluation of the integrals. For the numerical integration, the computational grid is translated vectorially by $(0.5\Delta x_1, 0.5\Delta x_2)$.

The numerical performance of the method is documented for three-dimensional computations of wave generation caused by a moving bottom. In these examples the computational domain is $L\times W = 300h\times 10h$, where h is the water depth. Various discretizations are tested.

The bottom shape and motion are given by $\delta(\boldsymbol{x},t)=\delta^t(t)\,\delta^x(\boldsymbol{x})$. The time dependence $\delta^t(t)$ is chosen on the form $\delta^t(t)=1-[\mathrm{e}^{-bt}/a][a\cos(at)+b\sin(bt)]$. This function allows for an exponential behavior, characterized by the parameter b, as well as oscillating behavior, characterized by the parameter a. From this form, we can express the linear solution of the problem by computing the corresponding linear wave elevation as described in Eq. (A.4). For practical purposes, we put $a=\pi/10$ and $b=10a$. This choice corresponds roughly to a pure exponential of the motion of the sea floor. The resulting function $\delta^t(t)$ is illustrated in Fig. 2a. In the following examples this choice of temporal evolution is kept while the function is varied.

We first simulate the generation of long-crested waves propagating along the numerical tank. The form $\delta^x(\boldsymbol{x})$ of the bottom motion is modeled by a square-shaped function as illustrated in Fig. 2b. The width of the displaced part of the bottom is 50 times the water depth along the x_1-direction (and 10 times the water depth along the x_2-direction). The form of the moving bottom is the same as in Hammack [17] who combined experimental measurements with linear analysis of the tsunami waves generated in a wave tank.

In the first numerical experiment the maximum vertical excursion of the moving part of the sea-floor is 15% of the water depth, i.e. $\delta_{\max}/h=0.15$. The simulations show how the wave train is generated and moves out of the generation zone (Fig. 3).

We study the convergence of the method where the prognostic equations (1) and (2) are integrated in time up to $t\sqrt{g/h}=100$, with solution of the Laplace equation obtained by the full equations (29) and (32). The latter are obtained by an iterative procedure which is initiated by first evaluating $V_{\mathrm{s}}^{(3)}$ from (28) and $\phi_{\mathrm{b}}^{(2)}$ from (27). These are inserted into (29) and (32). The improved estimates of V_{s} and ϕ_{b} – obtained explicitly without any equation solving – are then inserted into (29) and (32), obtaining improved values. This procedure is repeated once more. In all cases we have studied, the iteration has then converged, meaning that there is no gain by continuing the iteration.

We study the convergence of the amplitude of the leading wave crest after $t\sqrt{g/h}=100$, see Fig. 3, lower plot. The amplitude obtained from the fully nonlinear equations (29)–(32) is given for various resolutions in Table 1. The number of collocation points is $2N_1=1024$, 2048, 4096, and $2N_2=16$, 62, 64. The relative variation of the amplitude is less than one per mille. The results show a systematic convergence towards a non-dimensional value of the amplitude of 0.10224 (with a small deviation for the finest resolution in the lateral direction).

Next we test the computation of the amplitude, y_m, and position, $x_{1,m}$, of the leading crest at time $t\sqrt{g/h}=100$, comparing the full solution, obtained by Eqs. (29)–(32), to the approximation obtained by $V_{\mathrm{s}}^{(3)}$, given by the explicit formula (28). The approximations $V_{\mathrm{s}}^{(2)}$ given by (26), and $V_{\mathrm{s}}^{(1)}$ given by (24) are also tested. We evaluate the relative difference between the full solution and the various approximations, i.e.

$$\epsilon_{\mathrm{Amp.}}^{(n)}=\frac{|y_m(V_{\mathrm{s}}^{(n)})-y_m(V_{\mathrm{s}}^{\mathrm{full}})|}{y_m(V_{\mathrm{s}}^{\mathrm{full}})},$$

$$\epsilon_{\mathrm{Pos.}}^{(n)}=\frac{|x_{1,m}(V_{\mathrm{s}}^{(n)})-x_{1,m}(V_{\mathrm{s}}^{\mathrm{full}})|}{x_{1,m}(V_{\mathrm{s}}^{\mathrm{full}})}.$$

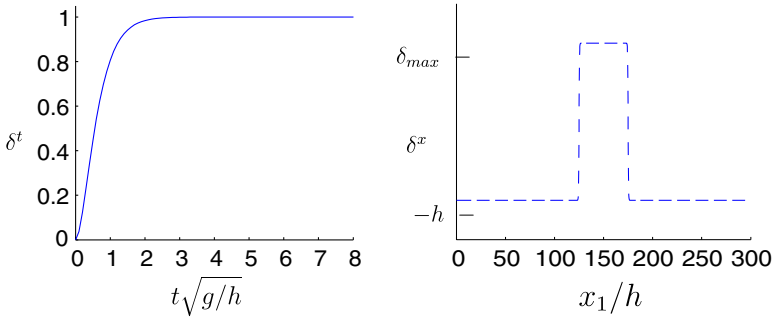

Fig. 2. Time and spatial dependence δ^t and δ^x for the bottom elevation where $\delta(\boldsymbol{x},t)=\delta^t(t)\delta^x(\boldsymbol{x})$.

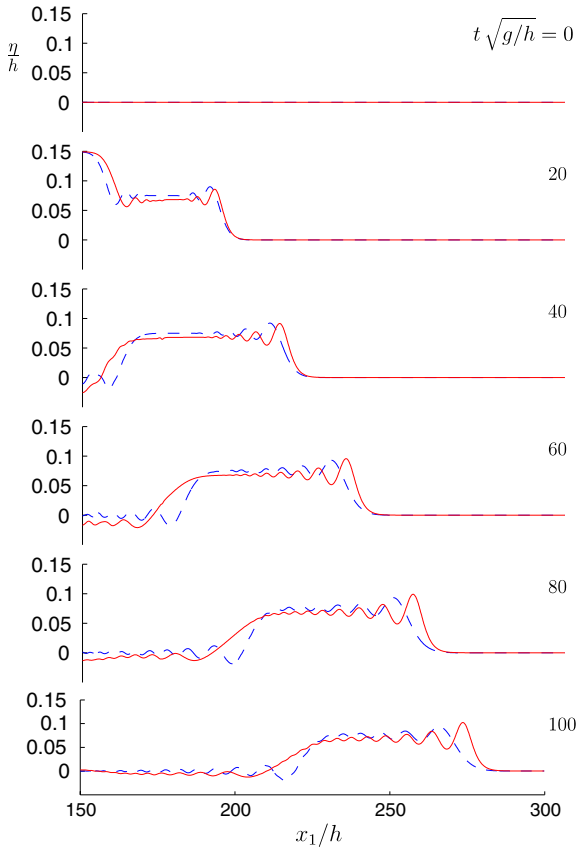

Fig. 3. Surface elevation due to a sudden rise of the bottom (as defined in Fig. 2). Surface at $t = \{0; 20; 40; 60; 80; 100\}\sqrt{h/g}$, fully nonlinear (—) and linear solution (––). $\delta_{\max}/h = 0.15$.

Table 1
Fully nonlinear amplitude of the wave front at $t\sqrt{g/h} = 100$ for several discretizations

$2N_2$	$2N_1$		
	1024	2048	4096
16	0.10230	0.10228	0.10224
32	0.10223	0.10224	0.10224
64	0.10220	0.10223	0.10220

$\delta_{\max}/h = 0.15$. Numerical wave tank: $300h \times 10h$ (length × width). Domain of local integration: $10h \times 10h$.

The results displayed in Table 2 – for $\delta_{\max}/h = 0.15$ – illustrate that $V_s^{(3)}$ approximates V_s^{full} with a relative error that is 0.0014 for the amplitude and 0.07×10^{-4} for the phase (position). The table illustrates, moreover, that $V_s^{(2)}$ approximates V_s^{full} quite well in this example, while $V_s^{(1)}$ gives only a coarse estimate. The various solutions are illustrated in Fig. 4.

Results from another simulation with larger nonlinearity, i.e. $\delta_{\max}/h = 0.2$, displayed in Table 3, illustrate that $V_s^{(3)}$ approximates V_s^{full} with a relative error that is 0.0012 for the amplitude and 2×10^{-4} for the phase (position). While $V_s^{(2)}$ gives a fairly good approximation the motion, the linear estimate (by $V_s^{(1)}$) is quite far from the full solution. The various solutions are illustrated in Fig. 5.

Calculations of the elevation and speed of the leading wave crest are shown in Fig. 6. The results illustrate that $V_s^{(3)}$ is very close to V_s^{full}, and that also $V_s^{(2)}$ provides a close match in this case, while the linear approximation $V_s^{(1)}$ models a different physics.

Table 2
Maximum-amplitude (y_m) and position ($x_{1,m}$) of the wave front at $t\sqrt{g/h} = 100$

V_s	Amp. (y_m)	Pos. ($x_{1,m}$)	$\epsilon^{(n)}_{\text{Amp.}}$	$\epsilon^{(n)}_{\text{Pos.}}$
$V_s^{(1)}$	0.09377	265.908	0.0828	0.0281
$V_s^{(2)}$	0.10253	273.644	0.0029	0.0002
$V_s^{(3)}$	0.10210	273.591	0.0014	0.0000
V_s^{full}	0.10220	273.589	–	–

$\delta_{\max}/h = 0.15$. Comparison between $V_s^{(1)}$ (given by Eq. 24), $V_s^{(2)}$ (given by Eq. 26), $V_s^{(3)}$ (given by Eq. 28), V_s^{full} (given by Eq. 29). All computations with $2N_1 = 4096$, $2N_2 = 64$. Evaluation of integral part corresponding to $V_s^{(R,2)}$ in Eq. (31) over $10h \times 10h$ (local integration).

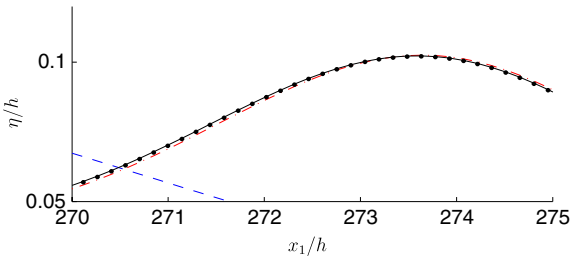

Fig. 4. Blow-up of Fig. 3 at $t = 100\sqrt{h/g}$. $(\delta_{\max} + h)/h = 0.15$. $V_s^{(1)}$ (––), $V_s^{(2)}$ (–·–), $V_s^{(3)}$ (···), fully nonlinear (—).

Table 3
Same as Table 2 but $\delta_{\max}/h = 0.2$

V_s	Amp. (y_m)	Pos. (x_m)	$\epsilon_{\text{Amp.}}$	$\epsilon_{\text{Pos.}}$
$V_s^{(1)}$	0.12497	265.908	0.1003	0.0349
$V_s^{(2)}$	0.13986	275.662	0.0069	0.0005
$V_s^{(3)}$	0.13873	275.564	0.0012	0.0002
V_s^{full}	0.13890	275.514	–	–

All computations with $2N_1 = 4096$, $2N_2 = 16$. Evaluation of integral part corresponding to $V_s^{(R,2)}$ in Eq. (31) over $10h \times 10h$ (local integration).

These tests illustrate that the formulation with $V_s^{(3)}$ represents an excellent approximation to solution of the Laplace equation. The relative difference between V_s^{full} and $V_s^{(3)}$ is very small. It is noted that the evaluation of $V_s^{(3)}$ is explicit and requires only the use of FFTs. Even for a maximum displacement of the bottom reaching 20% of the water depth, the relative error is of order 10^{-3} for the amplitude and 10^{-4} for the phase after a time which is hundred times $\sqrt{h/g}$. In dimensional terms, this corresponds to 33 min if the water depth is 4000 m and 16 min 40 s if the water depth is 1000 m.

The fast (FFT) version of the fully nonlinear, fully dispersive method is constituted by the prognostic equations (1) and (2) with V_s approximated by (28). This version is explicit. The linear part of (1) and (2) is inte-

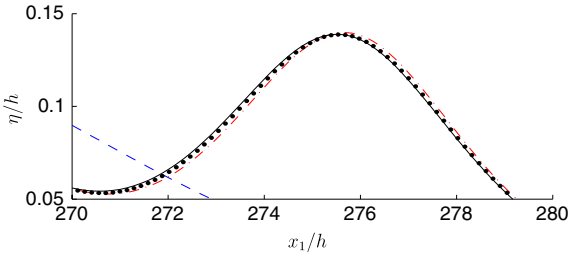

Fig. 5. Similar result as in Fig. 4 with $\delta_{\max}/h = 0.20$. $V_s^{(1)}$ (––), $V_s^{(2)}$ (–·–), $V_s^{(3)}$ (···), fully nonlinear (—).

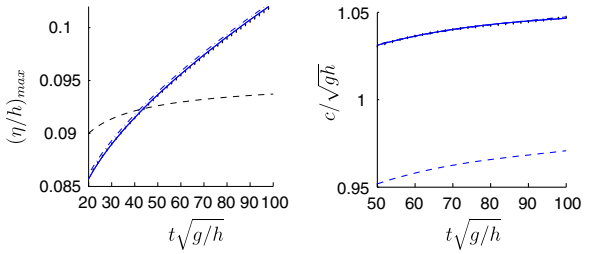

Fig. 6. Amplitude and speed of the front wave. $\delta_{max}/h = 0.15$. $V_s^{(1)}$ (––), $V_s^{(2)}$ (–·–),$V_s^{(3)}$ (···), fully nonlinear (—).

grated analytically in Fourier space (providing results to machine precision) while the nonlinear part of the equations are integrated by an RK-54 method as specified in Appendix A. Below we compare our method to published results for (i) the nonlinear wave field generated in a wave tank by the model of a slide, including state of the art nonlinear simulations of the waves, and (ii) the interaction between a steep solitary wave and a slope.

5. Waves generated by a submarine slide

The set of quasi two-dimensional laboratory experiments in scale 1:1000 as well as the complementary fully nonlinear and fully dispersive simulations were documented by Grilli et al. [14]. In the experiments a semi-elliptical shaped geometry with initial submergence of $d = 261$ m was moving down a slope, as visualized in Fig. 7. The figure indicates the location of the wave gauges that were used to record the experimental wave field above the slide.

In order to make consistent comparisons with the experiments and the simulations in [14], we choose exactly the same numerical parameters as in the original study. The bottom profile is taken identically as in their numerical setup, with a slope angle of $\theta = 15°$ and a total water depth of 1018.3 m. Moreover, the shelf is flat over 142.51 m with the bottom localized at $y = -76.37$ m. A semi-ellipse with thickness $T = 52$ m and length $B = 1000$ m simulates the slide and is moving downslope with an along-slope acceleration given by $\ddot{S}(t) = a_0[(\cosh(t/t_0))^{-2} - (\cosh(\alpha t/t_0))^{-2}]$ where $t_0 = 80$ s and $a_0 = 0.574$ m/s^2. The second term in the expression for the acceleration was chosen to correspond to a ramping function. By taking $\alpha = 50$, this leads to a ramping over approximately $t_0/20$ corresponding to the ramping chosen by Grilli et al. [14].

Our results are compared to the experiments and the simulations by Grilli et al. [14] where the results from the latter are interpolated from the digitized data from their Fig. 7. They documented an experimental $|\eta_{max}|_0 = 5.38$ at the gauge $g0$, while we find here a numerical value of $|\eta_{max}|_0 = 5.35$ at this position, which is a very close match. The spacial wave field predicted by the present method exhibits a very good agreement with the experimental data, see Fig. 8. This is also true for the time series at each of the gauges, see Fig. 9. It is evident that the present method provides results which are closely matching the experimental ones. A slight

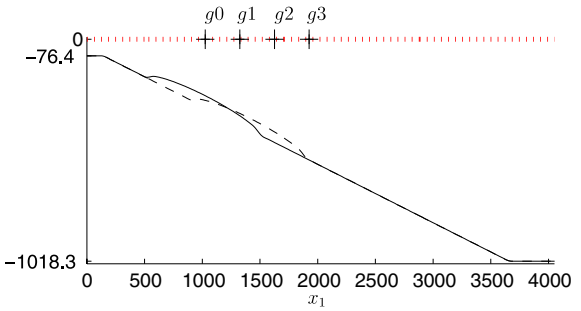

Fig. 7. Bottom elevation at $t = 0$ (—) and $t = 40$ s (––). The plus sign correspond to the location of the wave gauges in the experimental setup by Grilli et al. [14].

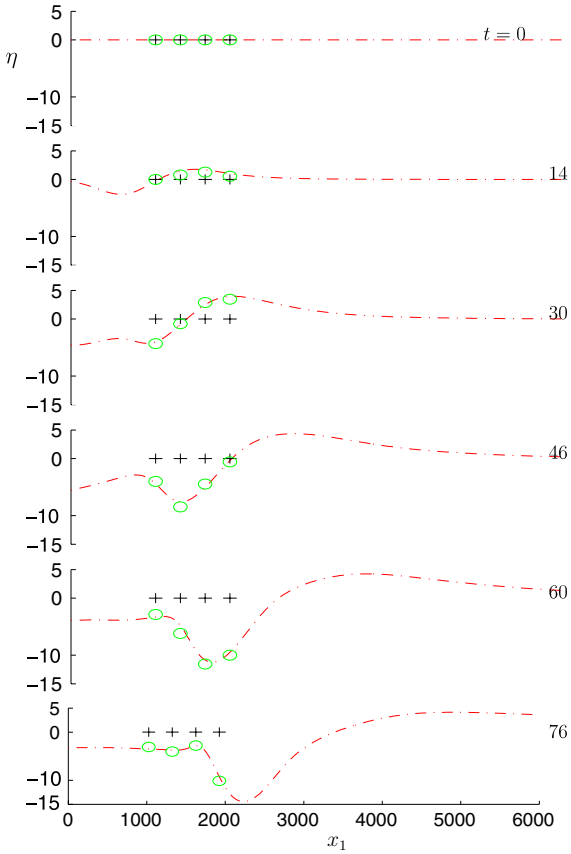

Fig. 8. Surface elevation due to a submarine landslide (as defined in Fig. 7). Free surface at $t = \{0; 14; 30; 46; 60; 76\}$, numerical (—) vs. experimental results by Grilli et al. [14] (○). The plus sign correspond to the location of the gauges as depicted in Fig. 7.

overprediction of the trough as compared to the method of Grilli et al. [14] can been seen on all gauges. This leads to a better match to experimental results, especially for the offshore gauges.

In order to more closely compare the computational efficiency between the present formulation and that used in [14], we have made runs using the same spatial discretization. Since the present method requires the bottom to be periodic, we have implemented a symmetric version of the method with respect to $x = 0$. The tank is hence considered to be twice as long as that used in [14]. It is discretized over 512 collocation nodes in the main direction and 4 points in the transverse, corresponding to $\Delta x_1 = 95$ m (as compared to $\Delta x_0 = 101.27$ m in [14]) and $\Delta x_2 = 100$ m. For this special comparison we have implemented a second-order constant time stepping Runge–Kutta scheme. This corresponds to the time stepping procedure used by Grilli et al. (This means that the time stepping procedure is the same as in Grilli et al. The difference is the procedure for the inversion of the Laplace equation, for which the speed is compared. The more accurate time stepping procedure, documented in Appendix A.1 is even faster, since longer time steps can be applied, because of the analytical integration of the linear part, and the use of the (variable) time-step control. The two different time-stepping procedures have been compared, and produce the same numerical results for non-dimensional time (t) up to 80.) Moreover, we choose the time step $\Delta t = 0.456$ s, identically as in their paper. This yields a constant Courant number of $Cr = 0.48$ and is similar to the one they used. We note that the time stepping procedure is not entirely identical, since Grilli et al. used a constant discretization along the actual free surface, while our is constant in the x_1,x_2-plane. Hence, taking a discretization which is somewhat finer and assuming the time step to be constant appears to be a fair way of comparing the numerical efficiency of the two codes. The total number of nodes in our simulations is 2048 and we perform computations on a Laptop with a 1.2 GHz P4M processor. The computing time per time step is obtained by an average over 10 runs of length

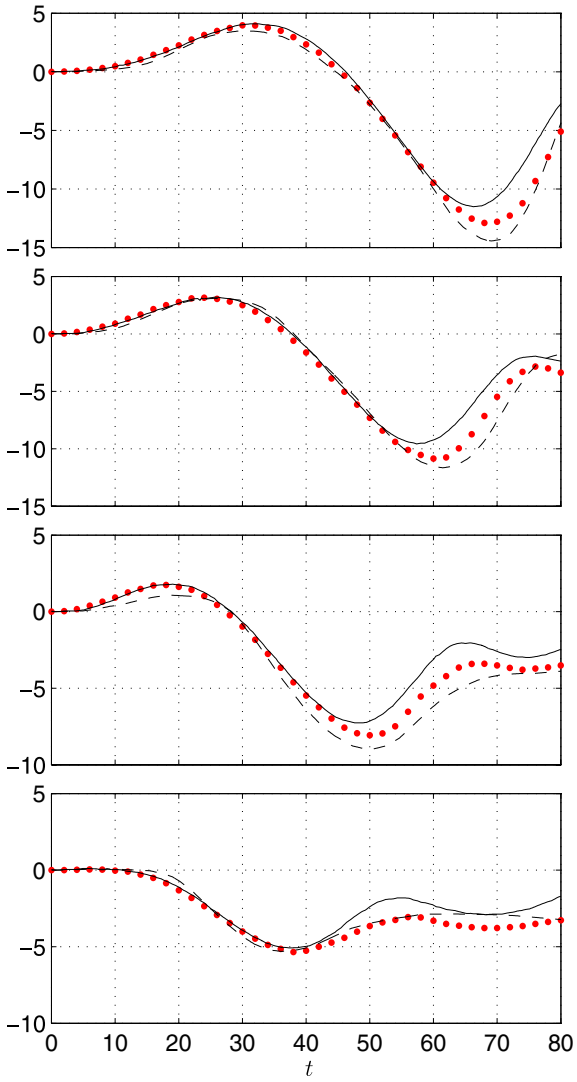

Fig. 9. Free surface elevation at the wave gauges $g0, g1, g2, g3$, numerical results from $V_s^{(3)}$ $(\cdots)$ as compared to laboratory $(--)$ and numerical $(—)$ experiments by Grilli et al. [14].

$176\Delta t$ each which showed little or no variation. We find that the computing time per time step is approximately 0.023 s while Grilli et al. [14] reported a computing time per time step of 404 s on a Mac G4-450 MHz. Since these architectures are somewhat equivalent (ours is actually a bit faster) we can compare directly the computing time, which is 18,000 times faster using the present method. This gain is easily explained, since the formulation we have derived and implemented is explicit, analytical and evaluated by FFT only.

6. Computations of shoaling

It is of interest to use the method to simulate the shoaling of the waves on a slope. Waves are computed up to the point of numerical (and physical) breaking. The present method (in three dimensions) is compared to the two-dimensional nonlinear simulations of shoaling solitary waves performed by Wei et al. [28]. They investigated the performance of a fully nonlinear Boussinesq model (in the figures referred to as FNBM) and compared to the extended Boussinesq model by Nwogu [22] (BM) and the fully nonlinear potential flow model by

Grilli et al. [13] (FNPF). Wei et al. studied the motion of three different solitary waves propagating up three different slopes. We shall here reproduce the case with slope 1:15, which is the steepest case where the fluid velocity is given, and use identically the same three input solitary waves as in [28], namely with amplitudes $H_0/h = 0.3$, 0.45 and 0.6 where H_0 denotes the wave amplitude and h the water depth outside the shelf-slope.

Fig. 10 shows half of the computational domain along the wave propagation direction. The input solitary waves were obtained from the exact method by Tanaka [29] and compared to the input waves in Wei et al. [28], without any distinguishable difference in the results presented here. An example of the evolution of the solitary wave with $H_0/h = 0.3$ over the slope is presented in Fig. 10 at several times of the simulation. In the simulations the reference depth is put to $h/2$. Two discretizations are used, viz. $\Delta x_1/h = 0.13$, 0.065 and $\Delta x_2/h = 0.3$. The waves are computed up to numerical breaking. More precisely, the wave profile at $t\sqrt{g/h} = 11$ exhibits a rise of the energy at high wavenumbers in the wavenumber space, see Fig. 11. It is important to note that in the numerics, the breaking is independent of the numerical resolution, and thus models physical steepening towards physical breaking.

Results for the nondimensional wave amplitude H/h_v are presented in Fig. 12, where H denotes the crest height of the solitary wave and h_v the water depth beneath the crest. Three different degrees of nonlinearity (i.e. solitary wave amplitude) are considered and compared to results from the three models used in Wei et al. [28] who simulated the waves up to the point of numerical breaking. We have digitized Figs. 5c and 7c in [28] for subsequent extraction of the data and comparison to the simulations using the present model. It can be seen from the plots that the present formulation provides a very good match concerning wave amplitude evolution for the highly nonlinear cases in the simulations.

The degree of nonlinearity in the simulations is also indicated by comparing the maximal fluid velocity at the wave crest and the wave speed. Our simulations show that the two quantities become almost equal in the end of the simulation, with the fluid velocity being as large as 90% of the wave speed before the computations are stopped (Fig. 13). Our results for the fluid velocity compare well with the fully nonlinear 2D simulations of Grilli et al. [13] almost up to breaking. We note that in the present simulations no smoothing or regridding are applied. The numerical results for the wave speed agree with the Boussinesq model but predict somewhat

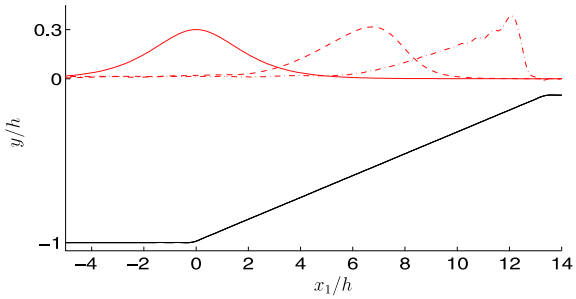

Fig. 10. Bottom topography and surface elevation for the shoaling of a solitary wave of initial elevation $H_0/h = 0.30$ over a slope $s = 1{:}15$. Elevation at $t\sqrt{g/h} = 0$ (—), $t\sqrt{g/h} = 6$ (– –) and $t\sqrt{g/h} = 11$ (–·–).

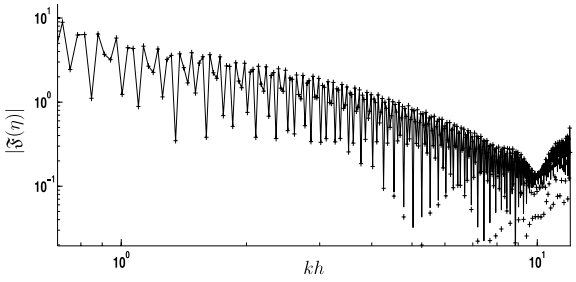

Fig. 11. Spectrum $|\Im(\eta)|$ at $t\sqrt{g/h} = 11$ in Fig. 10, with $\Delta x_1 = 0.13h$ (solid line) and $\Delta x_1 = 0.065h$ (+ + +).

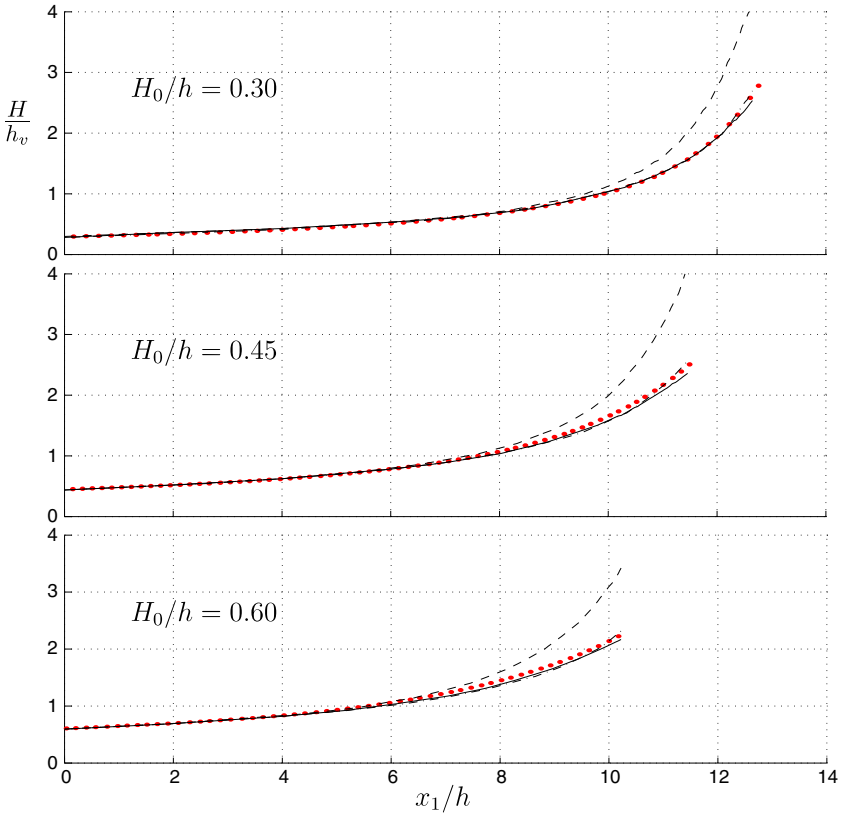

Fig. 12. Comparison between FNLP (—), BM (– – –), FNBM (–·–) from Wei et al. [28] and the present method with $V_s^{(3)}$ (···). Shoaling on a slope 1:15.

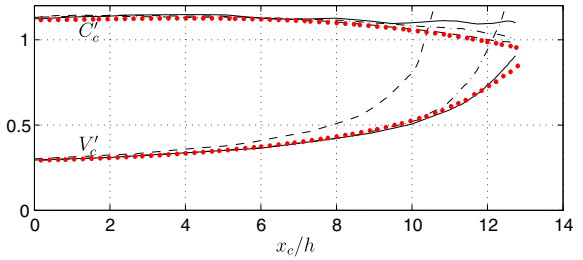

Fig. 13. Comparison between FNLP (—), BM (– – –), FNBM (–·–) from Wei et al. [28] and the present method with $V_s^{(3)}$ (···) of wave crest celerity C_c' and particle velocity V_c' at the crest for the solitary wave depicted in Fig. 12a.

smaller values than the fully nonlinear 2D code. The simulations with our model with the V_s replaced by $V_s^{(3)}$ illustrate the usefulness of the method up to the point where the waves are breaking.

7. Conclusion

We have derived a fully nonlinear and fully dispersive method to simulate the interaction between free surface flows and an uneven and/or moving bottom topography. The three-dimensional method assumes potential flow and is useful to simulate wave fields of large amplitude over the whole range of wavenumbers. The linear part of the prognostic equations (1) and (2) is integrated analytically in time providing results to machine precision while the nonlinear part is integrated using an RK-54 method with variable step-size con-

trol. The nonlinear normal velocity of the free surface is obtained by Eq. (28). No smoothing or regridding are applied. A partially dealiased scheme using zeros padding of the spectra is implemented. The formulation enables fast simulations of the nonlinear and dispersive wave fields over bathymetry of appreciable variation, or the waves caused by the tectonic or slide generated motion of the sea floor, in three dimensions. The code is useful to predict the nonlinear shoaling almost up to physical breaking. The latter is evidenced by the growing wave induced fluid velocity that becomes equal to the wave speed (for the long waves). The wave profile exhibits a rise of the energy at high wavenumbers in the wavenumber space. In the numerics, the breaking is independent of the numerical resolution, and thus represents the physics involved.

The derivations in this paper have been motivated by needs for improved representation of the dispersion effects in models for the strongly nonlinear interaction between the surface waves and variable bottom topography in space and time. On the onset, our method is similar to the fully nonlinear Green function method implemented and tested out by Grilli et al. [14]. It departs from the latter on one important point, however. The coupled integral equations (4) and (14) that result from the Laplace equation are here brought on a form where the dominant, leading contribution is explicit and is evaluated by fast Fourier transform (Eq. 28). Moreover, the resulting expressions are simple and useful for analytical manipulations. Practice documents that the explicit FFT-part of the solution captures the essential part of the wave field. The method reproduces the experimental elevation resulting from the slide motion in a wave tank. A direct comparison of the computing time shows that the present method is significantly faster than what has been documented by Grill et al. (in this example 18,000 times faster).

The efficiency of the method makes possible the computation of realistic tsunami waves over appreciable parts of the sea. This includes the transformation of the wave field due to strongly variable topography, e.g. in the transition from the deep to shallow regions, where the water depth may also be strongly oscillating. The full representation of nonlinearity and dispersion is important in the accurate prediction of solitary waves which may emerge in the shallow sea, as observed in the Strait of Malacca (Pelinovsky, personal communication). The waves may be computed up to the shore line where transparent dampers are needed to close the formulation (see e.g. [6]). The onshore flow may be obtained by long wave methods (see e.g. [24]).

Acknowledgments

The authors acknowledge Dr. Didier Clamond for numerous useful and stimulating discussions. This work was conducted under the Strategic University Program 'Modelling of currents and wave for sea structures' funded by the Research Council of Norway.

Appendix A

A.1. Time stepping procedure

The prognostic equations (1) and (2) can be rewritten by extracting their linear part and by taking their Fourier transform, deriving the following skew-symmetric form: $\hat{F}_t + \breve{A}\hat{F} + \hat{B} = \hat{N}$, where

$$\hat{F} = \begin{pmatrix} k\mathfrak{F}(\eta) \\ \frac{k\omega}{g}\mathfrak{F}(\phi) \end{pmatrix}, \quad \breve{A} = \begin{bmatrix} 0 & -\omega \\ \omega & 0 \end{bmatrix}, \quad \hat{B} = \begin{pmatrix} -\frac{k}{\cosh kh}\mathfrak{F}(V_b) \\ 0 \end{pmatrix}, \tag{A.1}$$

$\omega = \sqrt{gk\tanh kh}$ and $\hat{N}$ corresponds to the nonlinear contribution. The term $\hat{B}$ corresponds to the linear contribution from the moving bottom. The linear part of the prognostic equations is integrated analytically, implying the introduction of an integrating factor (see [4, p. 265]):

$$\hat{F}(k,t) = \exp[\breve{A}(t_0 - t)]\hat{G}(k,t) - \int_{t_0}^{t} \exp[\breve{A}(t' - t)]\hat{B}(k,t')\,\mathrm{d}t', \tag{A.2}$$

$$\hat{G}(k,t) = \exp[\breve{A}(t - t_0)]\hat{F}(k,t) + \int_{t_0}^{t} \exp[\breve{A}(t' - t_0)]\hat{B}(k,t')\,\mathrm{d}t', \tag{A.3}$$

which yields the equation $\hat{G}_t = \exp[\breve{A}(t - t_0)]\hat{N},\ \hat{G}(k,t_0) = \hat{F}(k,t_0)$.

This nonlinear system is integrated via a six-stages fifth-order Runge–Kutta scheme. The time stepping is controlled by the use of an embedded fourth-order scheme (Dormand and Prince, see [16]). In addition, a special "PI step size control" technique is used for the stabilization of the time step [16, IV Section 2].

If we neglect the nonlinear terms, then the following linear solution is obtained

$$\begin{aligned}\mathfrak{F}(\eta)(k,t) &= \mathfrak{F}(\eta)_0\cos(T) + \frac{\omega}{g}\mathfrak{F}(\phi)_0\sin(T) + \frac{1}{\cosh kh}\int_{t_0}^{t}\mathfrak{F}(V_{\mathrm{b}})(k,t')\cos(t')\,\mathrm{d}t',\\ \mathfrak{F}(\phi)(k,t) &= \mathfrak{F}(\phi)_0\cos(T) - \frac{\mathfrak{g}}{\omega}\mathfrak{F}(\eta)_0\sin(T) - \frac{g}{\omega\cosh kh}\int_{t_0}^{t}\mathfrak{F}(V_{\mathrm{b}})(k,t')\sin(t')\,\mathrm{d}t',\end{aligned} \tag{A.4}$$

where $\mathfrak{F}(\eta)_0 = \mathfrak{F}(\eta)(k,t_0)$, $\mathfrak{F}(\phi)_0 = \mathfrak{F}(\phi)(k,t_0)$, $T = \omega(t-t_0)$ and $T' = \omega(t-t')$. If the bottom motion starts from rest at $t_0 = 0$, then the linear expression (A.4) for the surface elevation yields Hammack's equation [17].

A.2. Remaining integrals

Introducing

$$D_0 = \frac{\eta'-\eta}{R},\quad D_1 = \frac{\eta'+\eta}{R_1},\quad D_2 = \frac{\delta'-\eta}{R_2},\quad D_3 = \frac{\delta'+\eta}{R_2},$$

where $\eta' = \eta(\boldsymbol{x}',t)$, $\eta = \eta(\boldsymbol{x},t)$, $\delta' = \delta(\boldsymbol{x}',t)$, $\delta = \delta(\boldsymbol{x},t)$, $R = |\boldsymbol{x}'-\boldsymbol{x}|$, $R_1^2 = R^2+4h^2$ and $R_2^2 = R^2+h^2$, the remaining integrals are:

$$N^S(V_{\mathrm{s}}) = \frac{1}{2\pi}\int V'_{\mathrm{s}}\left(\frac{1}{\tilde{r}}+\frac{1}{\tilde{r}_{\mathrm{B}}}-\frac{1}{R_1}-\frac{1}{R}+\frac{D_0^2}{2R}+\frac{2hD_1}{R_1^2}-\frac{D_1^2}{R_1}\left(\frac{-1}{2}+\frac{6h^2}{R_1^2}\right)\right)\mathrm{d}x'$$

$$\begin{aligned}T^S(\phi_{\mathrm{s}}) &= \frac{1}{2\pi}\int \phi'_{\mathrm{s}}\left(\frac{1}{\tilde{r}^3}-\frac{1}{R^3}\right)[\mathbf{R}\cdot\nabla'\eta' - (\eta'-\eta)]\,\mathrm{d}x'\\ &\quad + 1/2\pi\int\phi'_{\mathrm{s}}\left\{\mathscr{K}_{T2}[\mathbf{R}\cdot\nabla'\eta' - (\eta'+\eta)-2h] + \frac{D_1^2}{R_1^3}\left(\frac{-3}{2}+\frac{30h^2}{R_1^2}\right)[\mathbf{R}\cdot\nabla'\eta' - (\eta'+\eta)]\right\}\mathrm{d}x'\end{aligned}$$

$$N^B(V_{\mathrm{b}}) = \frac{1}{2\pi}\int -V'_{\mathrm{b}}\left(\frac{1}{\tilde{r}}+\frac{1}{\tilde{r}_{\mathrm{B}}}-\frac{2}{R_2}-\frac{h(D_2-D_3)}{R_2^2}-\frac{D_2^2+D_3^2}{R_2}\left(\frac{-1}{2}+\frac{3h^2}{2R_2^2}\right)\right)\mathrm{d}x'$$

$$\begin{aligned}T^B(\phi_{\mathrm{b}}) &= \frac{1}{2\pi}\int\phi'_{\mathrm{b}}\{(\mathscr{K}_{T\mathscr{B}1}+\mathscr{K}_{T\mathscr{B}2})[\mathbf{R}\cdot\nabla'\delta'-\delta'] + (\mathscr{K}_{T\mathscr{B}1}-\mathscr{K}_{T\mathscr{B}2})(\eta+h)\}\,\mathrm{d}x'\\ &\quad + 1/2\pi\int\phi'_{\mathrm{b}}\left(\frac{-3}{R_2^5}+\frac{15h^2}{R_2^7}\right)\left\{(\mathbf{R}\cdot\nabla'\delta'-\delta'+h)(\delta'^2+\eta^2)+\eta(\delta'-\eta)\right\}\mathrm{d}x'\end{aligned}$$

$$S^B(V_{\mathrm{s}}) = \frac{1}{2\pi}\int V'_{\mathrm{s}}\left\{\frac{1}{\tilde{r}}+\frac{1}{\tilde{r}_{\mathrm{C}}}-\frac{2}{R_2}-\frac{2h\delta}{R_2^3}\right\}\mathrm{d}x'$$

$$P^B(\phi_{\mathrm{s}}) = -\frac{1}{2\pi}\int\phi'_{\mathrm{s}}\left\{\left(\frac{1}{\tilde{r}^3}+\frac{1}{\tilde{r}_{\mathrm{C}}^3}-\frac{2}{R_2^3}\right)[\mathbf{R}\cdot\nabla'\eta'-\eta'] + \left(\frac{1}{\tilde{r}^3}-\frac{1}{\tilde{r}_{\mathrm{C}}^3}+\frac{6h\eta'}{R_2^5}\right)(\delta-h)\right\}\mathrm{d}x'$$

$$M^B(V_{\mathrm{b}}) = \frac{1}{2\pi}\int V'_{\mathrm{b}}\left[\frac{1}{R}+\frac{1}{R_1}-\frac{1}{\tilde{r}}-\frac{1}{\tilde{r}_{\mathrm{C}}}-2h\frac{\delta'+\delta}{R_1^3}\right]\mathrm{d}x'$$

$$\begin{aligned}D^B(\phi_{\mathrm{b}}) &= \frac{1}{2\pi}\int\phi'_{\mathrm{b}}\left\{2\delta\left(\frac{1}{\tilde{r}_{\mathrm{C}}^3}+\frac{1}{\tilde{r}^3}-\frac{1}{R^3}-\frac{1}{R_1^3}\right)[\mathbf{R}\cdot\nabla'\delta'-(\delta'-h)]\right\}\mathrm{d}x'\\ &\quad - 1/2\pi\int\phi'_{\mathrm{b}}\left\{\left(\frac{1}{\tilde{r}_{\mathrm{C}}^3}-\frac{1}{\tilde{r}^3}+\frac{1}{R^3}-\frac{1}{R_1^3}\right)(\delta-h)+12h^2\frac{\delta'+\delta}{R_1^5}\right\}\mathrm{d}x',\end{aligned}$$

where

$$\mathscr{K}_{T_2} = \frac{1}{\tilde{r}_{\mathrm{B}}^3} - \frac{1}{R_1^3} + \frac{6hD_1}{R_1^4} - \frac{D_1^2}{R_1^3}\left(\frac{-3}{2} + \frac{30h^2}{R_1^2}\right) \cdot \mathscr{K}_{T_{\mathscr{B}}1} = \left[\frac{1}{\tilde{r}^3} - \frac{1}{R_2^3} - \frac{3hD_2}{R_2^4} - \frac{D_2^2}{R_2^3}\left(\frac{-3}{2} + \frac{15h^2}{2R_2^2}\right)\right],$$

$$\mathscr{K}_{T}\mathscr{B}2 = \left[\frac{1}{\tilde{r}_{\mathrm{B}}^3} - \frac{1}{R_2^3} + \frac{3hD_3}{R_2^4} - \frac{D_3^2}{R_2^3}\left(\frac{-3}{2} + \frac{15h^2}{2R_2^2}\right)\right].$$

References

[1] M.J. Ablowitz, A.S. Fokas, Z.H. Musslimani, On a new nonlocal formulation of water waves, J. Fluid Mech. 562 (2006) 313–343.

[2] Y. Agnon, P.A. Madsen, H.A. Schäffer, A new approach to high order Boussinesq models, J. Fluid Mech. 399 (1999) 319–333.

[3] W.J.D. Bateman, C. Swan, P.H. Taylor, On efficient numerical simulation of directionally spread surface water waves, J. Comput. Phys. 174 (2001) 277–305.

[4] J.P. Boyd, Chebyshev and Fourier Spectral Methods, Dover, 2001.

[5] D. Clamond, J. Grue, A fast method for fully nonlinear water wave computations, J. Fluid Mech. 447 (2001) 337–355.

[6] D. Clamond, D. Fructus, J. Grue, Ø. Kristiansen, An efficient model for three-dimensional surface wave simulations. Part II: generation and absorption, J. Comput. Phys. 205 (2005) 686–705.

[7] W. Craig, C. Sulem, Numerical simulation of gravity waves, J. Comput. Phys. 108 (1993) 73–83.

[8] I.V. Fine, A.B. Rabinovich, R.E. Thomson, E.A. Kulikov, Numerical modeling of tsunami generation by submarine and subareial landslides, Submarine Landslides and TsunamisNATO Science Series, Series IV: Earth and Environmental Sciences, vol. 21, Kluwer Academic Publishers, Dordrecht, 2003, pp. 69–88.

[9] D. Fructus, D. Clamond, J. Grue, Ø. Kristiansen, An efficient model for three-dimensional surface wave simulations. Part I: free space problems, J. Comput. Phys. 205 (2005) 665–685.

[10] D. Fructus, C. Kharif, M. Francius, Ø. Kristiansen, D. Clamond, J. Grue, Dynamics of crescent water wave patterns, J. Fluid Mech. 537 (2005) 155–186.

[11] D.R. Fuhrman, P.A. Madsen, H.B. Bingham, A numerical study of crescent waves, J. Fluid Mech. 513 (2004) 309–342.

[12] R.S. Gibson, C. Swan, The evolution of large ocean waves: the role of local and rapid spectral changes. Proc. Roy. Soc. (in press).

[13] S.T. Grilli, J. Skourup, I.A. Svendsen, An efficient boundary element method for nonlinear water waves, Eng. Anal. Bound. Elem. 6 (1989) 97–107.

[14] S.T. Grilli, S. Vogelmann, P. Watts, Development of a 3D numerical wave tank for modeling tsunami generation by underwater landslides, Eng. Anal. Bound. Elem. 26 (2002) 301–313.

[15] J. Grue, On four highly nonlinear phenomena in wave theory and marine hydrodynamics, Appl. Ocean Res. 24 (2002) 261–274.

[16] E. Hairer, G. Wanner, Solving ordinary differential equations II. Stiff and differential–algebraic problemsSpringer Series in Computational Mathematics, vol. 14, Springer, Berlin, 1991.

[17] J. Hammack, A note on tsunamis: their generation and propagation in an ocean of uniform depth, J. Fluid Mech. 60 (1973) 769–799.

[18] P.L.-F. Liu, T.-R. Wu, F. Raichlen, C.E. Synolakis, J.C. Borrero, Runup and rundown generated by three-dimensional sliding masses, J. Fluid Mech. 536 (2005) 107–144.

[19] P. Lynett, P.L.-F. Liu, A numerical study of submarine-landslide generated waves and run-up, Proc. R. Soc. Lond. A 458 (2002) 2885–2910.

[20] P.A. Madsen, Y. Agnon, Accuracy and convergence of velocity formulations for water waves in the framework of Boussinesq theory, J. Fluid Mech. 477 (2003) 285–319.

[21] P.A. Madsen, H.B. Bingham, H. Liu, A new Boussinesq method for fully nonlinear waves from shallow to deep water, J. Fluid Mech. 462 (2002) 1–30.

[22] O. Nwogu, An alternative form of the Boussinesq equations for nearshore wave propagation, J. Waterway Port Coast. Ocean Eng. 119 (1993) 618–638.

[23] E. Pelinovsky, Analytical models of tsunami generation by submarine landslides, Submarine Landslides and TsunamisNATO Science Series, Series IV: Earth and Environmental Sciences, vol. 21, Kluwer Academic Publishers, Dordrecht, 2003, pp. 111–128.

[24] E. Pelinovsky, R. Mazova, Exact analytical solutions of nonlinear problems of tsunami wave run-up on slopes with different profiles, Natural Hazards 6 (1992) 227–249.

[25] E. Pelinovsky, A. Poplavsky, Simplified model of tsunami generation by submarine landslides, Phys. Chem. Earth. 21 (12) (1996) 13–17.

[26] R.A. Smith, An operator expansion formalism for nonlinear surface waves over variable depth, J. Fluid Mech. 363 (1998) 333–347.

[27] K.M. Watson, B.J. West, A transport-equation description of nonlinear ocean surface wave interactions, J. Fluid Mech. 70 (1975) 815–826.

[28] G. Wei, J.T. Kirby, S. Grilli, R. Subramanya, A fully nonlinear Boussinesq model for surface waves. Part 1. Highly nonlinear unsteady waves, J. Fluid Mech. 294 (1995) 71–92.
[29] M. Tanaka, The stability of solitary waves, Phys. Fluids 29 (1986) 650–655.
[30] V.E. Zakharov, Stability of periodic wave of finite amplitude on the surface of a deep fluid, J. Appl. Mech. Phys. 2 (1968) 190–198 (Engl. Transl.).